Translational Oncology
www.transonc.com

Volume 3 Number 3 June 2010 pp. 181–194 181

Strategies for High-Resolution Imaging of Epithelial Ovarian Cancer by Laparoscopic Nonlinear Microscopy[1]

Rebecca M. Williams*,[2], Andrea Flesken-Nikitin†,[2], Lora Hedrick Ellenson‡, Denise C. Connolly§, Thomas C. Hamilton§, Alexander Yu. Nikitin† and Warren R. Zipfel*

*Department of Biomedical Engineering, Cornell University, Ithaca, NY, USA; †Department of Biomedical Sciences, Cornell University, Ithaca, NY, USA; ‡Department of Pathology and Laboratory Medicine, New York Presbyterian Hospital–Weill Medical College of Cornell University, New York, NY, USA; §Ovarian Cancer Program, Fox Chase Cancer Center, Philadelphia, PA, USA

Abstract

Ovarian cancer remains the most frequently lethal of the gynecologic cancers owing to the late detection of this disease. Here, by using human specimens and three mouse models of ovarian cancer, we tested the feasibility of nonlinear imaging approaches, the multiphoton microscopy (MPM) and second harmonic generation (SHG) to serve as complementary tools for ovarian cancer diagnosis. We demonstrate that MPM/SHG of intrinsic tissue emissions allows visualization of unfixed, unsectioned, and unstained tissues at a resolution comparable to that of routinely processed histologic sections. In addition to permitting discrimination between normal and neoplastic tissues according to pathological criteria, the method facilitates morphometric assessment of specimens and detection of very early cellular changes in the ovarian surface epithelium. A red shift in cellular intrinsic fluorescence and collagen structural alterations have been identified as additional cancer-associated changes that are indiscernible by conventional pathologic techniques. Importantly, the feasibility of *in vivo* laparoscopic MPM/SHG is demonstrated by using a "stick" objective lens. Intravital detection of neoplastic lesions has been further facilitated by low-magnification identification of an indicator for cathepsin activity followed by MPM laparoscopic imaging. Taken together, these results demonstrate that MPM may be translatable to clinical settings as an endoscopic approach suitable for high-resolution optical biopsies as well as a pathology tool for rapid initial assessment of ovarian cancer samples.

Translational Oncology (2010) 3, 181–194

Introduction

Ovarian cancer is the deadliest gynecologic cancer and the fifth leading cancer in cancer-related deaths in women in the United States. It will be responsible for approximately 21,550 (3% of total) of new cancer cases and 14,600 (5% of total) of cancer-related deaths in 2009 [1]. When the disease is diagnosed at its early stages, the survival rate can be higher than 90%. However, because the early stages are relatively asymptomatic, most cases of ovarian carcinomas are not identified until late, rarely curable stages when almost 70% of tumors have already spread beyond the ovary [2]. Cytoreductive surgery of metastatic ovarian cancer may extend the patient's survival, but its success greatly depends on effective detection and elimination of the bulk of tumor [3–5].

Development of new imaging diagnostic approaches is expected to significantly advance detection of ovarian cancer. Several recent studies have reported on improved detection of metastatic ovarian cancer by multitargeted *in vivo* optical imaging [6] and fluorescence protease imaging in immunocompromised mice [7]. Unfortunately,

Address all correspondence to: Alexander Yu. Nikitin, Department of Biomedical Sciences, Cornell University, T2 014A VRT Campus Rd, Ithaca, NY 14853-6401. E-mail: an58@cornell.edu; or Warren R. Zipfel, Department of Biomedical Engineering, B45 Weill Hall, Cornell University, Ithaca, NY 14853. E-mail: wrz2@cornell.edu

[1]This work was supported by National Institutes of Health grants CA112354, CA96823, and RR17595 (to A.Y.N.); CA116583 and P41-RR04224 (to R.M.W. and W.R.Z.); and P50 CA083638 (to D.C.C., T.C.H., and A.Y.N.).

[2]These authors contributed equally.

Received 9 October 2009; Revised 22 December 2009; Accepted 29 December 2009

 1944-7124/10/$25.00
DOI 10.1593/tlo.09310

resolution of these approaches has precluded evaluation of neoplasms at the cellular level. Furthermore, feasibility of intravital detection of earlier stages of ovarian cancer has not been demonstrated.

A possible approach to address both issues is nonlinear imaging by multiphoton microscopy (MPM) and second harmonic generation (SHG). MPM is a type of incoherent nonlinear laser scanning microscopy that uses the simultaneous absorption of two near-infrared (NIR) photons to excite an electronic transition equivalent to the absorption of a single higher energy, "bluer" photon [8,9]. Use of (NIR) light instead of UV or higher energetic bands, which are required to excite most intrinsic emitters in biological tissues [10–12], mitigates UV-associated photodamage, optical aberrations, and excitation light attenuation. These advantages, together with absence of out-of-focal plane excitation, allow MPM to penetrate approximately two-fold deeper into optically scattering tissues with much cleaner subcellularly resolved images compared with confocal microscopy (see reviews by Zipfel et al. [9] and Helmchen and Denk [13]). MPM is frequently used simultaneously with SHG, an imaging strategy based on nonlinear coherent scattering of the illumination light by asymmetric macromolecular tissue components, such as collagen. SHG always emits at exactly one-half of the illumination wavelength and is easily separated from the broad generally blue fluorescence emission spectra characteristic of unstained tissue, enabling simultaneous imaging of collagen at the single fibril level [12].

Owing to MPM's features, such as depth of penetration, reduced phototoxicity, and intrinsic optical sectioning, and SHG's high-resolution assessment of fibrillar collagen structure not visible in standard hematoxylin and eosin (H&E)–stained sections, these nonlinear imaging methods have been recognized as promising approaches for cancer diagnostics [12]. Optical biomarkers of ovarian cancer were specifically evaluated with nonlinear microscopy [14]. However, it remains unclear to what extent MPM/SHG imaging will allow for robust identification of routine diagnostic pathological features. Furthermore, the applicability of MPM/SHG to characterization of various stages of ovarian carcinogenesis in autochthonous mouse models of cancer has not been tested. Most importantly, it is unknown whether there is adequate sensitivity to identify features *in vivo*, making the feasibility of practical high-resolution endoscopic MPM/SHG uncertain.

In this article, we assess of applicability of the MPM/SHG approach to pathological evaluation of epithelial ovarian carcinoma (EOC) in human samples and three syngeneic mouse models generated by us. We demonstrate that MPM of intrinsic tissue fluorescence in ovarian tissues allows reproducible identification of neoplastic features such as cellular atypia and architectural alterations at different stages of carcinogenesis. This information is further complemented by MPM/SHG–specific features such as cancer-associated alterations in intrinsic fluorescence and collagen structure. Finally, we demonstrate, in a proof-of-principle experiment, that high-resolution MPM/SHG optical biopsy can be accomplished by *in vivo* laparoscopy with a miniature stick objective lens. This approach can be further combined with prescreening for neoplastic changes by a cathepsin-activated NIR fluorescent probe.

Materials and Methods

Mouse Models of Ovarian Cancer

Development of EOC in mice expressing Simian virus (SV) 40 T antigen under control of the Mullerian inhibitory substance receptor 2 promoter (Tg*MISIIR-TAg*) was described previously [15].

Induction of EOC by a single transinfundibular intrabursal administration of recombinant adenovirus-expressing Cre (AdCre) in mice carrying floxed copies of *p53* and *Rb* genes was also described elsewhere [16].

To prepare a syngeneic mouse model of disseminated peritoneal EOC- a *p53*-, and *Rb*-deficient FVB/N ovarian surface epithelium (OSE) cell line OSN1 [17] was transduced with LNCX2 retrovirus containing mouse c-Myc (kind gift from Dr Andrew Yen). Briefly, retrovirus was produced by EcoPack2-293 (protocol PT3132-1; Clontech Laboratories, Palo Alto, CA), and exponentially growing cells were exposed to a medium containing 50% retroviral supernatant and 8 μg/ml polybrene (S2667; Sigma, St. Louis, MO) for 24 hours. The medium was changed for complete growth medium, and 500 μg/ml G418 (gentamicin sulfate; Cellgro, Sigma) was added 48 hours afterward. The resulting cell line OSN3 was intraperitoneally inoculated into 5- to 6-week-old FVB/N inbred mice (Taconic, Hudson, NY) at a concentration of 1×10^7 cells/0.5 ml of PBS. Mice injected with 0.5 ml of PBS only were used for control.

At scheduled time points or on signs of illness, the animals were either anesthetized or killed, and their tissues were processed for *in vivo* or *ex vivo* imaging, respectively, followed by histologic processing and pathological assessment as described later. As a control for morphologic alterations during imaging, a part of some specimens was directly processed for histologic analysis. In addition, a parallel identically treated group of animals was killed at the same time points and subjected to standard necropsy and processing procedures. All mice were maintained identically following recommendations of the Institutional Laboratory Animal Use and Care Committee.

Cell Culture

Preparations of primary normal and p53/Rb mutant OSE cells were performed as previously described [16–18]. Briefly, OSE cells were isolated by collagenase-dispase digestions of ovaries from mice carrying floxed copies of *p53* and *Rb* genes [16]. Cells were expanded within three passages, exposed to AdCre, and used after three passages. Complete Cre-*LoxP*–mediated gene excision was verified by polymerase chain reaction [16]. For control experiments, OSE cells were exposed to adenovirus-expressing β-galactosidase (AdLacZ).

Human Materials

Using anonymous fresh surgical material tagged for disposal, specimens of morphologically normal ovaries and serous EOC were collected at the Weill Medical College of Cornell University. One- to three-millimeter-thick slices of the material were prepared, immediately placed into either Ringer's solution or serum- and phenol red–free, HEPES-buffered RPMI and kept on ice. The material was transported to imaging facilities and used for collection of images by multiphoton microscope within 6 to 20 hours after resection. All procedures were approved by the institutional review board.

Nonlinear (MPM and SHG) Imaging of Intrinsic Fluorescence

Multiphoton imaging was accomplished as previously described [12,19,20]. Briefly, a 780-nm uncompensated beam from a modelocked Ti:sapphire laser (Tsunami pumped with a Millennia Xs; Spectra Physics, Mountain View, CA) was directed through a Pockels Cell (350-80LA; Conoptics, Danbury, CT) with laboratory-built electronics for beam modulation and blanking during scan fly-back. The beam was then directed into a modified BioRad scanner (MRC-600,

Hercules, CA) interfaced with a modified (fixed stage) Olympus AX-70 upright microscope (Center Valley, PA). Specimens were imaged either with a standard objective (20×/0.95W XLUNPlanFl; Olympus) or with an endoscopic stick objective (27×/0.7W IV-OB35F22W20; Olympus). Tissue emissions were separated from the excitation beam using a 670DCXRU long-pass dichroic filter (Chroma Technology, Inc, Rockingham, VT) placed directly at the back aperture of the microscope objective. The emissions were subsequently separated into two channels with a 440DCXRU long-pass dichroic and HQ390/702-2P and BGG22 emission filters (Chroma Technology, Inc). The first channel (355-425 nm, pseudocolored blue in the figures) is designed for collecting second harmonic from fibrillar collagen and the second channel (~450-550 nm, pseudocolored yellow) collects emissions from tissue intrinsic fluorescence such as cellular NAD(P)H and retinoid compounds. Both signals were detected using blue bialkali-photocathode PMT assemblies (HC125-02; Hamamatsu, Bridgewater, NJ). For determining intrinsic fluorescence color—long-wavelength (LW) *versus* short-wavelength (SW) emission—signals were instead separated using a 500DCXRU dichroic splitter to BGG22 (SW) and 580DF150MP (LW) emission filters (Chroma Technology, Inc). All imaging on freshly excised mouse samples occurred within 15 minutes after removal.

Analysis of collagen fibril alignment in the peritoneum was analyzed by calculating two-dimensional fast Fourier transforms (FFTs) of high-resolution SHG image stacks (164 × 110 × 10 μm^3). The resulting Fourier images were fit to two-dimensional Gaussian surfaces, and their asymmetry was defined as the ratio of major to minor axes. Image stacks were collected from the peritoneum around tumors of two EOC mice (n = 4 stacks) and in two control mice (n = 4 stacks).

Quantitative Assessment of Intrinsic Fluorescence: Intensity, Color, and Anisotropy

For quantification of intensity, color, and steady-state emission anisotropy of the intrinsic fluorescence in cell cultures, cell regions were automatically defined by pixel intensities greater than the measured image background plus the image SD. In tissue explants, cells of interest were masked manually using the paint tool and an additional channel in Adobe Photoshop (San Jose, CA). All pixel tabulation routines were custom-written using the IDL data analysis environment (ITT Visual Information Solutions, White Plains, NY).

For anisotropy measurements, the excitation polarization was adjusted for linear polarization (~50/1 ellipticity) directly after the objective by means of a Berek compensator (5540; New Focus, San Jose, CA) placed before the scanning box. The emitted fluorescence was separated into parallel and perpendicular components after the collecting objective with a broadband polarizing beam splitter (10FC16PB.3; Newport, Irvine, CA) and two polarizers (5511; New Focus) placed immediately before the emission filters (BGG22; Chroma Technology, Inc). The fluorescence anisotropy A was defined as the normalized difference between the emission intensities parallel ($I_\parallel$) and perpendicular ($I_\perp$) to the exciting polarization:

$$A = \frac{I_\parallel - I_\perp}{I_\parallel + 2I_\perp}$$

Calibration of the relative detected efficiencies ($I'_\parallel$ and $I'_\perp$) was accomplished by rotating the excitation polarization so that the parallel channel became the perpendicular channel and *vice versa*. For an isotropic sample, the measured anisotropy is the same with both excitation polarizations so that:

$$A = \frac{I'_\parallel - gI'_\perp}{I'_\parallel + 2I'_\perp} = A_{\text{rot}} = \frac{I'_{\parallel\text{rot}} - (1/g)I'_{\perp\text{rot}}}{I'_{\parallel\text{rot}} + 2I'_{\perp\text{rot}}}$$

This relationship was used to determine g, the relative scaling factor between the two channels accounting for differential emission path efficiencies, and PMT gain variations. Average anisotropy values for the masked regions were calculated by an algorithm written within IDL.

Quantification of red shift in cellular intrinsic fluorescence of tissues was accomplished by masking normal OSE or tumor regions in images from the disseminated metastasis mouse model. Average pixel values from the LW *versus* SW channels from those regions were tabulated using a custom-written algorithm within IDL.

In Vivo Imaging

The mouse to be imaged was shaved and anesthetized in an induction chamber with 3.5% isoflurane gas. After 1 to 2 minutes, it was transferred to the imaging stage where gas was delivered through a 0.5-inch-diameter tube with a small opening to insert the mouse snout, and warming was accomplished with a heating pad with feedback from a rectally inserted probe monitoring core temperature (FHC model 40-90-8C A720D). Gas percentage was adjusted to 1% to 2%, maintaining a ~60/min breathing rate as described previously [21]. For imaging with a standard water immersion objective (Olympus XLUNPlanFl 20×/0.95 W), a Parafilm bed was suspended over the mouse as a platform to isolate the ovary from mouse breathing motions. The ovary was threaded through an incision in the abdomen and a precut opening in the suspended Parafilm bed. Immersion saline necessary for optimal imaging was kept around the ovary by the Parafilm bed.

Imaging directly into the mouse abdomen was accomplished using the 3.2-mm-diameter Olympus stick objective lens (IV-OB35F22W20 27×/0.7 W). In addition to the microprobe optic, two other developments were required for obtaining high-quality cellularly resolved tumor images within the abdominal cavity: 1) a mechanism for flushing blood and other optically unfavorable, tissue-derived substances away from the imaging region, and 2) a mechanism for stabilizing the tissues from mouse movements. We initially designed a sleeve through which the microprobe slid for focusing; the sleeve was connected to perfusion piping and provided stabilization to the tissue. This design turned out to be too bulky and drew the tissue into it when the probe was moved away from the specimen. A simpler design in which a small tube (2 mm in diameter) was mounted on a separate micromanipulator proved better for flushing tissues in the field of view. The hose also acted to stabilize the tissue, reducing tissue motion due to mouse breathing and objective focusing.

Imaging of Cathepsin Activity

For administering ProSense 680 (VisEn Medical, Inc, Woburn, MA), mice were anesthetized with Avertin (2.5% vol./vol. in 0.85% NaCl; 0.020 ml/g body weight), and the ProSense 680 was injected into a tail vein at 2 nmol/150 µl in PBS. Mouse tissues were imaged *ex vivo* 24 hours after ProSense 680 administration. Overall fluorescence images were collected using the RFP2 filter on an Olympus SZX12 fluorescence stereomicroscope. Multiphoton imaging of ProSense 680 was accomplished as previously described for intrinsic fluorescence,

except that the fluorescence emission was instead split by a 560DCXRU into blue- (BGG22; Chroma Technology, Inc) and red- (650DF100MP; Chroma Technology, Inc) pseudocolored channels. The blue emission was detected with a bialkali PMT (HC125-02; Hamamatsu) and the NIR ProSense 680 emission (pseudocolored red in the figures) was detected using a red-sensitive GaAsP photocathode PMT (H7422P-40; Hamamatsu) with custom-designed amplifier circuitry. ProSense 680 imaging required significantly (typically fivefold) less excitation power than that for imaging intrinsic fluorescence.

Pathological Assessment

Human and mouse specimens were labeled by ink for orientation, placed into PBS-buffered 4% paraformaldehyde, fixed overnight, and processed for paraffin embedding. Before sectioning, samples were carefully oriented to ensure direct comparison of MPM/SHG and routine microscopic images. Prepared sections were stained with H&E and evaluated under a light microscope. All ovarian lesions were identified according to the Classification Guidelines endorsed by the Mouse Models of Human Cancer Consortium [22,23] and World Health Organization's classification of human ovarian cancer [24]. Histologic images were collected by SPOT-RT or Insight cameras (Diagnostic Instruments, Sterling Heights, MI) and compared with MPM/SHG images of the same or parallel specimens.

Morphometric Analysis

Digital MPM images of z series with 5-μm steps were imported into SPOT software (v. 4.6; Diagnostic Instruments). Comparable areas of optical sections across OSE covering the corpus luteum were identified, and nuclear and cytoplasmic contours were manually marked by individuals who were blinded to the experimental parameters. Image overlays were recorded and parameters calculated using the *measurements* function.

Statistical Analysis

For statistical analysis, two-sided unpaired Student's *t* tests were performed using InStat 3.05 and Prism 4.03 software (GraphPad, Inc, La Jolla, CA).

Results

High-Resolution Multiphoton Microscopy of Intrinsic Fluorescence in Mouse and Human Ovarian Cancer

Previously, we demonstrated that histologic architecture of the normal ovary and its cellular composition can be accurately identified by MPM of intrinsic fluorescence of freshly excised samples [12]. Therefore, to determine the value of MPM for pathological assessments of neoplastic lesions, we compared images taken with MPM/SHG without added fluorescent labels with those from sections after routine histologic processing and H&E staining of the normal OSE and its neoplasms (both mouse and human). As visualized using H&E staining, normal OSE presented as a single layer with squamous morphology (Figure 1*A*). In contrast, ovarian carcinomas of Tg*MISIIR-TAg* mice (n = 12) contained densely packed polygonal atypical epithelial cells (Figure 1*D*). In agreement with our previously reported observations [15], the neoplastic cells were arranged in solid sheets and separated by a limited stroma. MPM/SHG imaging of fresh unstained tissues provided the same level of resolution in terms of the overall histologic and cellular features of the normal (Figure 1, *B* and *C*) and neoplastic tissues (Figure 1, *E* and *F*). Similar to H&E staining, neoplastic features, such as high nuclear-cytoplasmic ratios, variations in cell sizes and altered tissue architecture were easily identifiable. MPM/SHG imaging also allowed better visualization of collagenous stroma (Figure 1, *B*, *C*, *E*, and *F*) and demonstrated that most collagen fibers near the invasive edge are located perpendicular toward its surface (Figure 1, *E* and *F*). At the same time, H&E sections were essential for evaluation of key pathological characteristics such as nucleoli, chromatin condensation, and overall tinctorial properties of tissues. Identification of mitotic and apoptotic cells was also problematic with MPM/SHG alone.

To extend the generality of these observations, we developed and evaluated a new model of disseminated peritoneal EOC. In this model, OSE transformed by *p53* and *Rb* inactivation and c-Myc overexpression form multiple neoplastic tumors on the visceral and parietal walls of the abdominal cavity 3 to 5 weeks after intraperitoneal injection. Similar to neoplasms of Tg*MISIIR-TAg* mice, neoplastic cells were identified by both H&E and MPM/SHG imaging (Figure 1, *G* and *H*) in all 10 studied cases. Notably, these tumors also had an aberrant appearance and orientation of collagen (Figure 1, *H* and *I*). Fibrils underlying normal peritoneal mesothelium were relatively uniform and had a wavy appearance, whereas those around tumor masses had variable diameter and a straight-rigid appearance. Uniformity and appearance aberrations were well discernable (at low and high resolutions, respectively) by projecting optical slices from a collagen image stack underlying mesothelium (Figure 1, *J* and *K*) or neoplastic cells (Figure 1, *L* and *M*). Alignment properties were automatically analyzed by computing FFTs of the projected images and fitting Gaussian ellipses to the resulting Fourier components. FFTs from normal (Figure 1*N*) and carcinomatous (Figure 1*O*) peritoneum image stacks revealed a significant increase in asymmetry (P = .0456) of the tumor fibrils with respect to normal fibrils (mean ± SE; 3.0 ± 0.6, n = 4 *vs* 1.49 ± 0.02, n = 4). A potential difference in segmental collagen indicative of fibrillogenesis (observable as micrometer-scale spots in the images, see Williams et al. [25]) was also investigated. Collagen segments were hypothesized to be more numerous in the cancer tissues owing to an increased collagen turnover in these tissues (see, e.g., Kenny and Lengyel [26]). However, the amount of observable segmental collagen was found to be fairly equivalent in the cancer and control tissues.

We next tested the application of MPM/SHG to human samples. Comparative analysis of normal ovary (Figure 2, *A* and *B*, n = 8) and ovarian adenocarcinomas (Figure 2, *C* and *D*, n = 4) confirmed that this approach provides a level of detail similar to that obtained with standard histologic processing, with previously noted advantages and limitations. Consistent with observations in mouse models and studies in human tissues [14], collagen from human EOC tumors was generally observed in thicker, less uniform bands than that from normal ovaries (Figure 2, *D vs B*).

MPM-Based Morphometric Analysis Allows Detection of Early Changes during Ovarian Carcinogenesis

According to literature reports, in humans, early ovarian lesions can be identified according to their morphometric parameters, such as enlarged cellular and nuclear size [27–31]. However, because identification of such lesions is usually accompanied by ovariectomy, their progression to carcinoma remains unconfirmed. To reproducibly examine early events associated with ovarian carcinogenesis, we turned

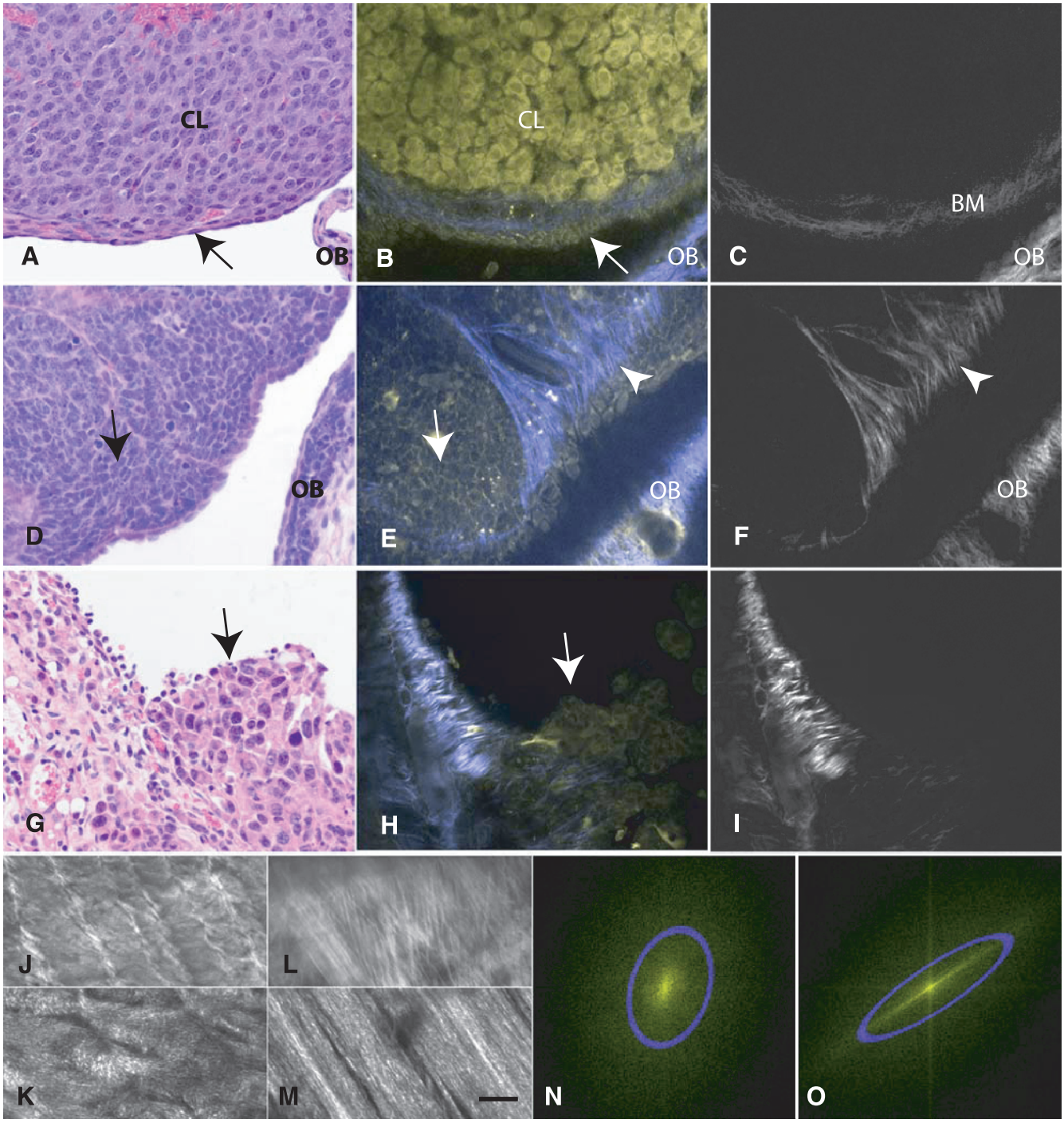

Figure 1. Evaluation of MPM (yellow) and SHG (blue and grayscale) potential for examination of mouse EOC. Normal mouse ovary (A–C), ovarian carcinomas of Tg*MISIIR-TAg* (D–F), and disseminated peritoneal EOC (G–M) mouse models were visualized by H&E staining (A, D, and G). MPM intrinsic emission (B, E, and H) and SHG imaging (B, C, E, F, H, I–M). (A–C) The ovarian surface epithelium (OSE, arrow), part of the corpus luteum (CL), and the ovarian bursa (OB) are all clearly resolvable by MPM and resemble those in conventional histologic image. In addition, SHG demonstrates collagen in the ovarian bursa and the basement membrane (BM) underneath of OSE. (D–F) Monomorphous polygonal neoplastic cells (arrow) are detectable by H&E and MPM. Note that SHG demonstrates presence of collagen with most collagen fibers near tumor periphery being located perpendicular toward its surface (arrowhead), a feature not evident in conventionally prepared tissue. (G–H) A group of neoplastic cells (arrow) invading the parietal peritoneum. Low- (J and L) and high- (K and M) magnification projection images of collagen architecture from normal peritoneum (J and K) and around tumor regions (L and M). (N and O) Representative Fourier transforms from the full images shown in K and M, respectively. Gaussian ellipses (blue) are fit to determine the collagen fibril asymmetry. MPM images were acquired using 780-nm excitation. Blue and yellow pseudocolors represent 355 to 425 nm and 450 to 550 nm emissions, respectively. For clarity, the SHG images are reproduced in gray in C, F, and I to M. Scale bars: 30 μm (A–C), 22 μm (D–F), 45 μm (G–I, J, and L), and 12 μm (K and M).

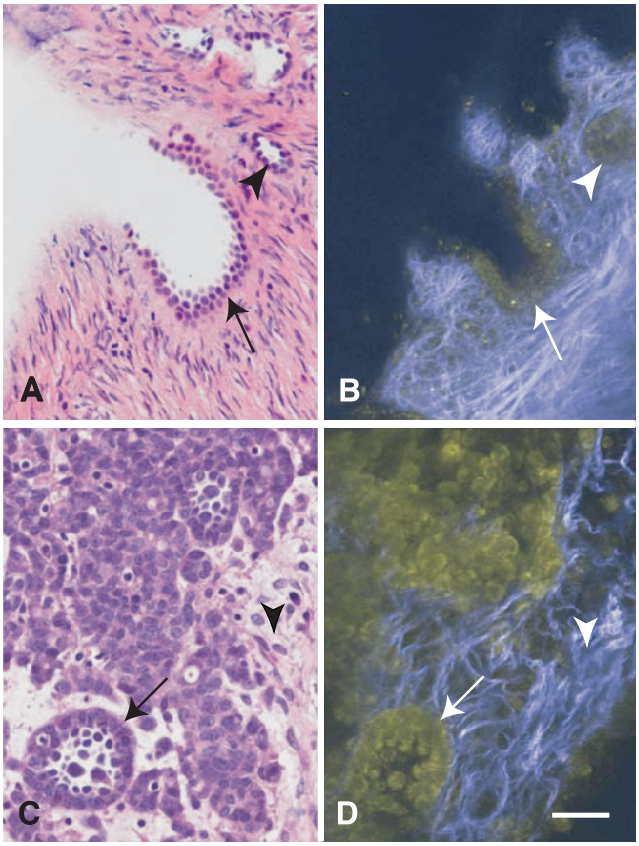

Figure 2. Standard histology and MPM/SHG of human ovarian epithelium and poorly differentiated adenocarcinoma. The same tissue specimens were visualized after formalin fixation and paraffin embedding followed by H&E staining (A and C) and before fixation using MPM/SHG of intrinsic tissue emissions (B and D). (A, B) Morphologically normal ovarian epithelium in the invaginations (arrow) and simple cysts (arrowhead) near the surface of the ovary. (C–D) Atypical neoplastic cells forming glandular structure (arrow) within desmoplastic stroma (arrowhead). Note presence of collagen fibrils imaged via second harmonic generation (SHG; blue), a feature not readily evident in conventionally prepared tissue. MPM/SHG images are acquired as in Figure 1. Scale bar, 30 μm in all images.

to our model of serous ovarian adenocarcinoma initiated by conditional inactivation of OSE *p53* and *Rb* after a single transinfundibular intrabursal injection of AdCre [16]. This model is uniquely suited for such studies because of temporal and local control of the initiating event. EOC develop relatively synchronously and lead to death in 97% of mice with median survival of 227 days after gene inactivation [16].

Similar to other ovarian samples, neoplastic lesions discernable by pathological evaluation of H&E sections were readily detectable by MPM/SHG (Figure 3, *A* and *B*). Furthermore, MPM/SHG allowed detection of a thickening of the collagen fibers at or near the basement membrane underlying early dysplastic lesions (compare Figure 3, *C* and *D*, with Figure 1, *B* and *C*). After confirming our earlier observations that more than 90% of OSE cells are infected after administration of 5×10^7 pfu/µl of adenovirus (Figure 3*E* and Flesken-Nikitin et al. [16]), we next tested whether MPM/SHG optical sectioning could facilitate detection of morphologic alterations at 8 and 34 days after conditional inactivation of p53 and Rb. No changes in cellular morphology and histologic architecture were detected by visual evaluation of either H&E or MPM sections. However, a quantitative morphometric assessment of MPM sections taken in parallel to the ovarian surface demonstrated a significant enlargement of nuclei and cytoplasm of OSE 8 and 34 days after initiation of carcinogenesis (Figure 3, *F–H*). Interestingly, nuclear-cytoplasmic ratios were not changed to any significant extent (P = .6547 and P = .3761 at days 8 and 34, respectively).

Quantitative Changes in Intrinsic Fluorescence Properties of Ovarian Cancers

Because the intracellular fluorescence signal in epithelial cells is thought to derive primarily from NAD(P)H, we hypothesized that characteristics of this signal—intensity, spectrum, or anisotropy—may yield further information about the metabolic state of cells. We initially tested these parameters in primary OSE cells carrying floxed *p53* and *Rb* genes three passages after exposure to AdCre or AdLacZ (control). Indeed, intensity in cells with *p53*/*Rb* deletion was significantly lower (60 ± 4%, mean ± SE, n = 32 images) than that of the normal population (100 ± 12, n = 16 images, P = .0003). We also observed a slight spectral red shift in cell cultures (not shown). Both characteristic changes seemed correlated with a vesicular production of a fluorescent material not evident in the normal cells *in vivo*.

The third parameter tested was steady-state emission anisotropy of the intrinsic fluorescence signal. Such a measurement is expected to yield information about the amount of time the fluorophore has rotated with respect to its fluorescence lifetime. For example, the rotation time (and fluorescence lifetime) can change on NADH binding to a high–molecular weight protein. Intrinsic fluorescence anisotropy

Figure 3. Ovarian surface epithelium carcinogenesis associated with conditional inactivation of *p53* and *Rb* genes. Multilayered atypical cells forming papillary structures (arrows) can be identified by conventional microscopy (A) and MPM/SHG (B). Thickening of the collagen fibrils (arrowheads) near and at the basement membrane of early dysplastic lesion (arrow) is evident in the MPM/SHG image (C) with the SHG reproduced in grayscale for clarity (D). (E) Expression of eGFP in the OSE of a mouse ovary after a single ovarian intrabursal injection with 5×10^7 pfu/µl of AdCMVEGFP. *Arrow* indicates OSE; *CL*, corpus luteum; *F*, follicle; *V*, vessel. Green pseudocolor is GFP fluorescence and yellow is intrinsic fluorescence (<500 nm emission). (F) Morphometric evaluation of intrinsic emission images of mouse OSE. Size of individual cells and their nuclei and cytoplasm was assessed by estimation of area (white rings, μm^2, mean ± SE). (G) Results are plotted for images collected at 8 days after intrabursal administration of AdCMVCre (Cre) or AdCMVLacZ (LacZ) to p53floxPRb1floxP mice. Unpaired t test yielded 2-tailed P = .0002 for whole-cell Cre *versus* LacZ (171.4 ± 12.4, n = 45 *vs* 120.4 ± 6.0, n = 53), P = .0466 for nucleus Cre *versus* LacZ (74.8 ± 5.3, n = 45 *vs* 53.0 ± 10.7, n = 26), and P = .0009 for cytoplasm Cre *versus* LacZ (96.58 ± 8.7, n = 45 *vs* 65.6 ± 3.78, n = 53). (H) At 34 days after transformation, unpaired t test yielded 2-tailed P = .0007 for whole-cell Cre *versus* LacZ (130.4 ± 6.5, n = 40 *vs* 92.1 ± 8.8, n = 36), P = .015 for nucleus Cre *versus* LacZ (70.0 ± 4.5, n = 40 *vs* 53.4 ± 4.9, n = 36), and P = .0007 for cytoplasm Cre *versus* LacZ (60.38 ± 4.3, n = 40 *vs* 38.6 ± 4.3, n = 36). All experiments have been performed in duplicates, and yielded similar results. Scale bars, 15 µm (A, B), 20 µm (C, D), 30 µm (E), and 12 µm (F).

in neoplastic OSE cells (0.301 ± 0.001, mean ± SE, n = 25 images) was significantly (P < .0001) lower than that found in normal OSE cells (0.319 ± 0.003 mean ± SE, n = 25 images). These results may indicate that more metabolically active cells, such as neoplastic cells, have a higher fraction of free to bound NAD(P)H (as has been shown in transformed mammary cell cultures [32]).

However, in mice, we determined that intensity and anisotropy values were highly sensitive to tissue scattering and thus depended

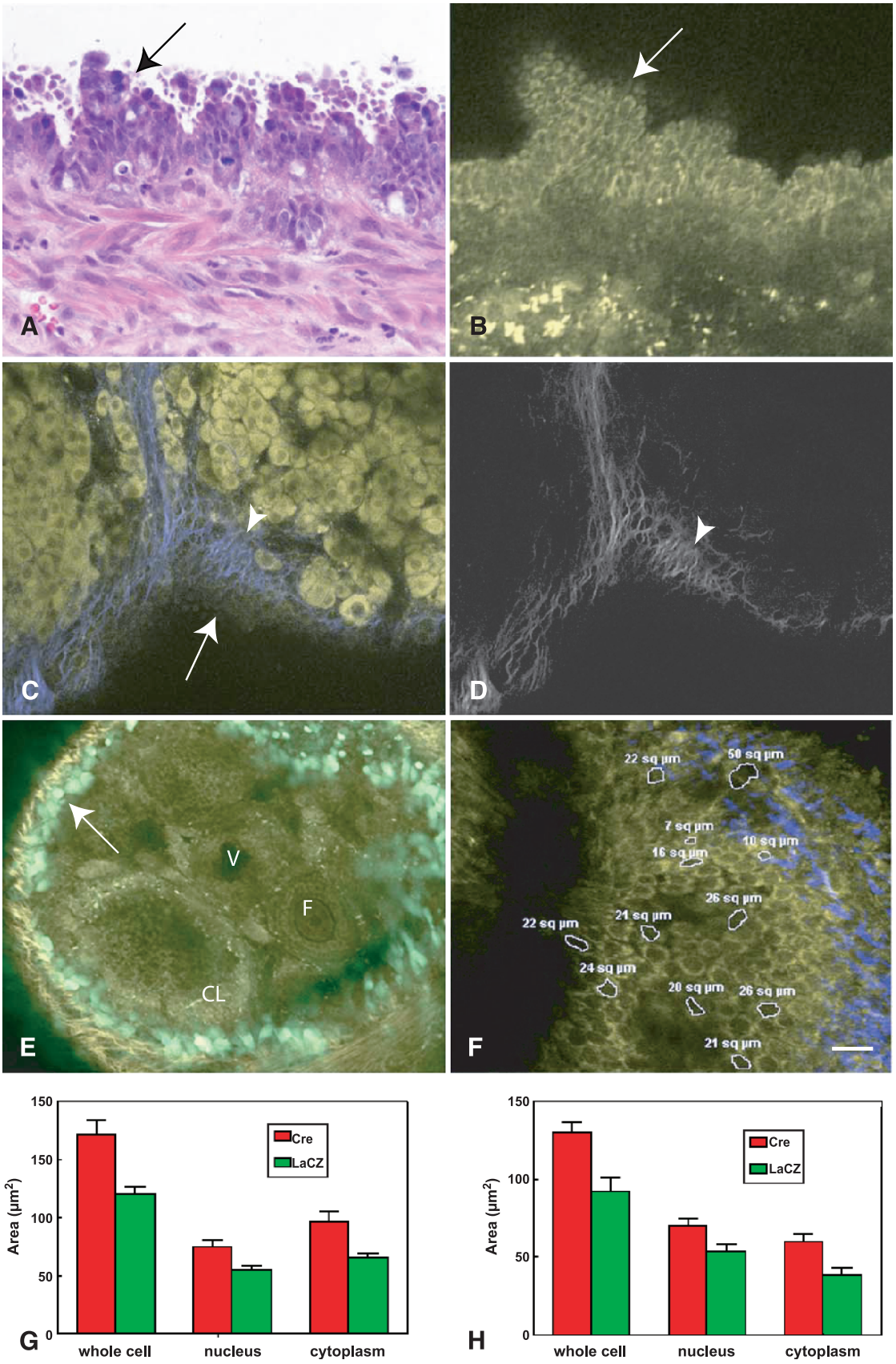

on the amount and type of tissue through which the image was obtained. Accordingly, intensity and anisotropy analyses of tissues have yielded inconsistent results (not shown).

At the same time, a red shift in the average cellular intrinsic fluorescence was reproducibly observed in tumor-derived cell masses compared with normal OSE. MPM images of freshly excised tissue from the disseminated metastasis model (Figure 4) exhibited an LW/SW ratio that was significantly higher in neoplastic *versus* normal cells (1.3 ± 0.1, mean ± SE, n = 7 tumors, *vs* 1.00 ± 0.03, n = 9 ovaries, P = .0064). Intriguingly, the spectral shift in tumors appeared to arise mainly from a separate population of red-emitting cells within the tumor mass (Figure 4*D*). These red-emitting cells were found to be viable by analysis of NADH intensity and costaining with the vital stain calcein-AM (data not shown).

Intravital MPM of Ovarian Cancer Using Laparoscopic Stick Objective

It has been previously demonstrated that under specific experimental conditions, usually in combination with research fluorophores, MPM may be used for imaging in living animals (e.g., see Zipfel et al. [9], Brown et al. [33], Condeelis and Segall [34]). To examine the feasibility for *in vivo* applications without contrast agents, we imaged ovaries from live mice (Figure 5, *A–F*) by exteriorizing the ovary to isolate it from the body cavity. This method was sufficient for resolving single OSE cells in unstained ovaries (Figure 5, *A–C*) and for discriminating these normal OSE from early EOC neoplasias using the floxed *p53/Rb* model (Figure 5, *D–F*).

However, standard large-diameter microscope objectives preclude access to internally located organs and tissues. In addition, to collect images at micrometer-scale resolution, strategies for mitigating motion artifacts primarily because of patient breathing must be in place. To address these challenges, we tested a microprobe "stick" objective recently developed by Olympus. This series of optics are fully aberration corrected objective lenses with small-diameter (1.2 and 3.2 mm) centimeter-long tips. We found simple GRIN lenses to be ineffective for the collection of high-quality intrinsic emission images due presumably to their more significant aberrations. In agreement with our previous results demonstrating the applicability of the Olympus microprobe objective for MPM imaging of intrinsic fluorescence of excised colon tissues [35], we could successfully image ovarian and peritoneal tissues without staining (not shown). After additional improvements for tissue rinsing and stabilization by supplementary tubing, we were able to image the parietal and visceral mesothelium and underlying tissues of the peritoneal cavity. Importantly, neoplastic cells were readily discernable from surrounding normal tissues in the mouse model of disseminated peritoneal EOC (Figure 6).

Combination of Low-Magnification Screening with High-Resolution MPM Optical Biopsy

A potential limitation of the stick objective lens is its small field of view. To facilitate intravital screenings of neoplastic lesions across large areas, mice were intraperitoneally injected with ProSense 680, a complex that emits red light on cathepsin B–mediated hydrolysis. In agreement with previous results [36], this indicator of protease activity has been effective in the detection of neoplastic disseminated peritoneal EOC cells by low magnification both with standard and multiphoton excitation (Figure 7, *A–D*). Selected areas were subsequently visualized by the laparoscopic objective lens (Figure 7, *E* and *F*), enabling visualization of individual cells with cathepsin B activity. Whereas most fluorescent cells were neoplastic cells, capillaries and intramuscular cells underneath of the parietal peritoneum (Figure 7*G*) were also detected in agreement with earlier observations [36]. MPM/SHG enabled a detailed mapping of the tumor boundary in three dimensions, confirming our earlier observations that collagen

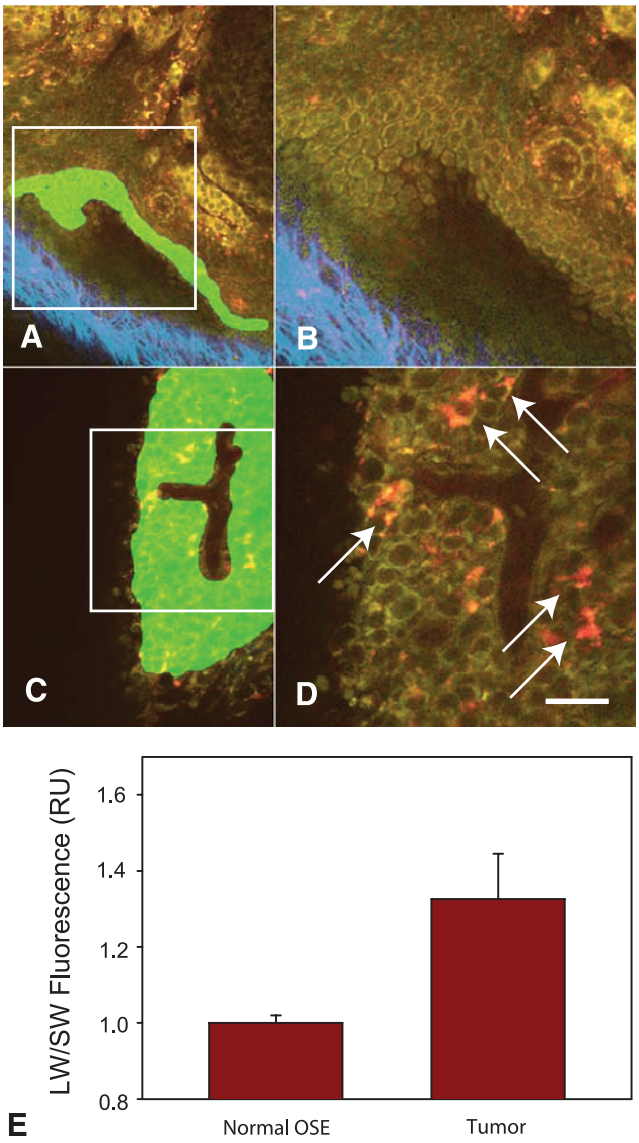

Figure 4. Emission color changes in intrinsic fluorescence of EOC. Normal OSE (A and B) and neoplastic cells from the disseminated peritoneal EOC model (C and D) were analyzed for the relative amounts of LW/SW (510-650 nm/410-490 nm, green/red pseudocolor) intrinsic fluorescence. For reference, SHG from the collagen of the ovarian bursa is shown in blue pseudocolor. Intrinsic fluorescence images of OSE are manually marked (green masked areas, A and C). The white boxes mark the zoomed regions shown in B and D, respectively. (E) Analysis of average pixel intensities in the green masked areas shows that tumor intrinsic fluorescence is red-shifted with respect to normal OSE owing to a distinct red-emitting cell population (arrows, D). Average LW/SW ratios are 1.00 ± 0.03 (mean ± SE, n = 9; RU, relative units) for normal OSE and 1.3 ± 0.1 (P = .0064, n = 7) for neoplasms. Data were acquired from 450 images at 780-nm excitation. Scale bars, 50 μm (A, C) and 25 μm (B, D).

fibrils around tumors were straighter and orientated toward the tumor boundary at the invasive front (Figure 7*H*).

Discussion

Minimally invasive or noninvasive methods of cancer diagnosis and therapeutic assessment in humans and real-time monitoring of carcinogenesis in experimental animals remain among the most coveted, challenging goals of cancer research. Undoubtedly, such abilities would tremendously facilitate our understanding of cancer initiation and progression, as well as enable development of patient-tailored therapeutic approaches. Two recent developments have provided an exciting premise for further studies. Firstly, there has been recent remarkable progress in technologies, allowing noninvasive imaging of molecular and cellular processes [37,38]. Secondly, technological progress in manipulating and genetically modifying the mouse genome has led to rapidly expanded repertoire of accurate cancer models that genetically and phenotypically mimic human cancers (reviewed in Jonkers and Berns [39], Van Dyke and Jacks [40], and Frese and Tuveson [41]).

Both advances have stimulated the evolution of fluorescent contrast agents for detection and monitoring of cancer [37,42]. Problems with these agents include reporter specificity, induced toxicity, and appropriate delivery strategies. Endogenous emitters, in contrast, are integral to the tissue. Although their photophysical characteristics are generally inferior (dim and emitting at short wavelengths that scatter easily in tissue), intrinsic tissue emissions exhibit signature properties of the natural tissue [12]. Because emission spectra are independent of the mode of excitation (i.e., conventional UV illumination *vs* two-photon excitation), the interpretation of multiphoton intrinsic tissue fluorescence images initially relies on a broad body of one-photon excitation tissue spectroscopy and imaging experiments (for reviews, see Ramanujam [10] and Richards-Kortum and Sevick-Muraca [11]), in which significant effort has been dedicated toward identifying spectral characteristics of intrinsic tissue that discriminate between normal and dysplastic or neoplastic tissues. Generally, empirical diagnostic criteria are established by analyzing the spectral shape of the intrinsic fluorescence excitation and/or emission curves by using a training set of cancerous *versus* normal specimens. This strategy has proven successful for a wide variety of cancerous tissues [43–53] and has been implemented in endoscopic devices for early detection of cancerous lesions in cervix [51], colon [52], bladder [43], skin [44], oral cavity [46,48,50], and esophagus [54]. Typically, spectral measurements are taken at a single point in the tissue, the location of which is guided by a white-light endoscope. Recently, however, imaging intrinsic fluorescence endoscopes have been developed (the LIFE-GI and Olympus

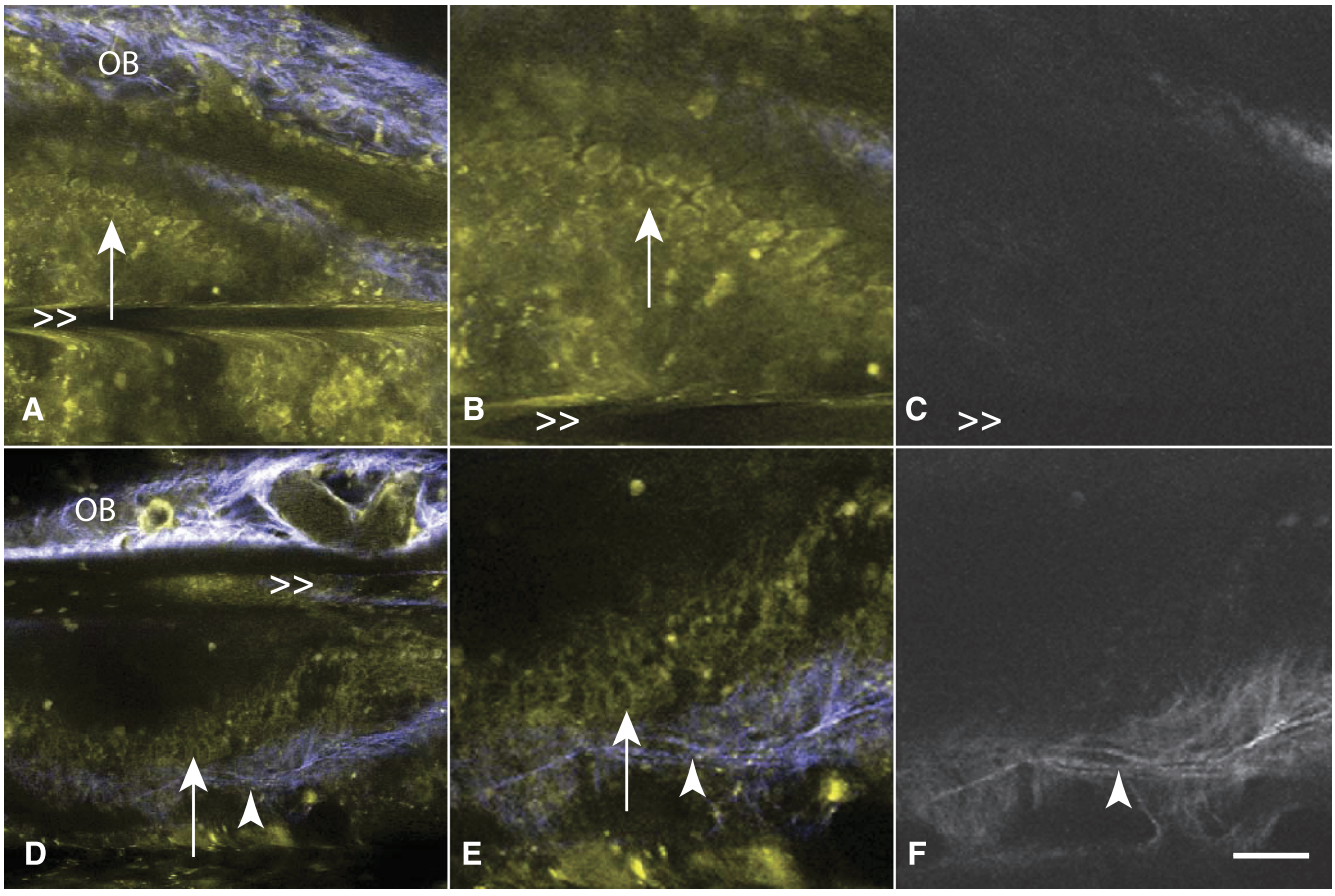

Figure 5. Discriminating normal from neoplastic OSE in live mice using MPM/SHG. Images of normal (A–C) and transformed (D–F) OSE mice from the conditional inactivation of *p53* and *Rb* model are acquired by exteriorizing the ovary and imaging with a standard objective lens. In zoomed images from A and D, respectively, OSE (arrows) are resolvable as a single layer in normal ovaries (B) and in multiple layers in neoplasia (E). In addition, the SHG channel (C, F) shows that the collagenous layer underneath of the OSE is visibly thicker in the neoplasia (arrowhead). OB marks the ovarian bursa and >> marks horizontal motion artifacts due to mouse breathing. Scale bars, 30 μm (A, D) and 15 μm (B, C, E, and F).

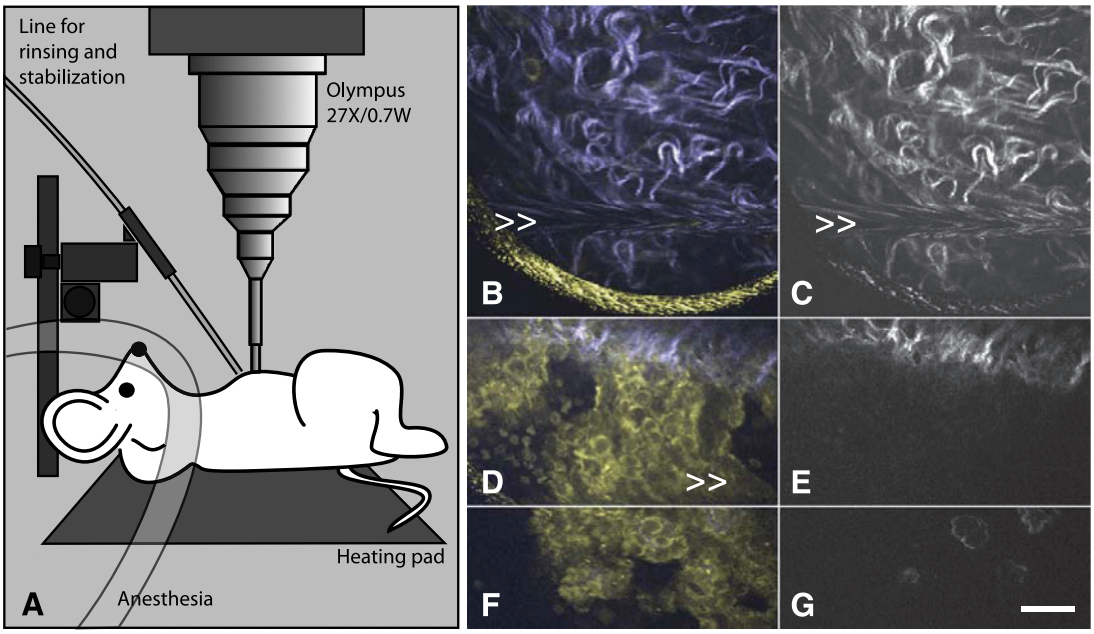

Figure 6. Intravital MPM/SHG imaging in the abdominal cavity using a microprobe objective lens (diagram, A). Normal peritoneum (B and C) and neoplastic cells of the disseminated peritoneal EOC model (D–G) imaged *in vivo* and *in situ* through an abdominal incision. Normal mesothelium is very thin, has low intrinsic fluorescence, and is essentially invisible using intravital MPM. However, neoplastic lesions are clearly visible at the invasive edge (D and E) and at the tumor surface (F and G). For clarity, SHG images are reproduced in grayscale in C, E, and G. Motion artifacts due to mouse breathing are marked with >>. The yellow meniscus at the bottom of B is the edge of field of view of the stick objective lens. Scale bar, 30 μm.

Auto-Fluorescence Videoscope systems) that show diagnostic potential for gastric [55], lung [56], and colon [57] cancers.

Albeit useful, the resolution of these systems is in the millimeter range, precluding detection and characterization of microscopic lesions as well as evaluation of tissue properties at the single-cell level. Nonlinear imaging approaches, such as MPM and SHG, have the potential to address this current limitation [9]. However, their applicability to clinical settings greatly depends on several advances including 1) the development of diagnostic criteria comparable to those obtained from routine histologic imaging, 2) the ability to obtain clear images in a difficult environment with significant optical scattering from blood [58] and motion artifacts from breathing and heart beat, 3) the development of endoscopic instruments compatible with ultrafast optics, enabling minimally invasive access to target organs and tissues, with high enough sensitivity to collect weak intrinsic fluorescence signals, and 4) improvements in the ability to locate regions for high-resolution assessment by MPM/SHG (better integration of the low- to high-magnification switch).

MPM/SHG Diagnostic Criteria

In the present study, we have tested the feasibility of MPM/SHG imaging in ovarian cancer, where the need for early diagnosis and thorough assessment of effectiveness of debulking surgery is of particular importance. Because the translation of new diagnostic tests and approaches into clinical practice, and particularly into pathology, greatly depends on the ability for linking new diagnostic criteria with already established and clinically proven sets of features, we have focused on advantages and disadvantages of imaging of native tissues with MPM compared with routine microscopy of H&E histologic slides. Side-by-side evaluation of EOC specimens from human patients and mouse models has demonstrated that MPM/SHG was sufficient to detect features of neoplasia such as size and shape of cellular compartments and tissue architecture. In addition, MPM/SHG images of tissue emissions provided information that was different to that obtained using standard histologic protocols. For instance, SHG clearly delineates fibrillar collagen structure, which is not visible in standard H&E sections. However, absent in MPM/SHG images were diagnostic nuclear information such as nucleoli size and shape, chromatin condensation, and localization. Furthermore, H&E color variations are also absent; cytosolic spaces are instead largely delineated by NAD(P)H fluorescence, which is sensitive to redox state [59].

The origins of many reproducible fluorescent features in the intrinsic tissue fluorescence images are still unknown. Our work contributes to the development of an atlas or database for interpreting intrinsic tissue emission changes characteristic of different lesions. Such efforts complement those by other laboratories [14,35,60–63].

In addition to the direct applicability of MPM/SHG imaging for diagnosis of neoplasia according to established pathological criteria, several of its intrinsic features are particularly attractive for facilitation of diagnosis. Firstly, MPM/SHG imaging allows rapid and three-dimensional pathological assessment of excised tissue with virtually no tissue preparation. This methodology should be useful in clinical situations requiring fast three-dimensional images of biopsies or in live tissue studies where tissue fixation cannot be used because it perturbs the tissue architecture or processes under study. We demonstrate here that MPM/SHG "optical sections" allow us to avoid time-consuming serial histologic sectioning required for the accurate evaluation of a single-layered OSE. It is anticipated that further studies using this approach will simplify morphometric assessments of early ovarian lesions in humans.

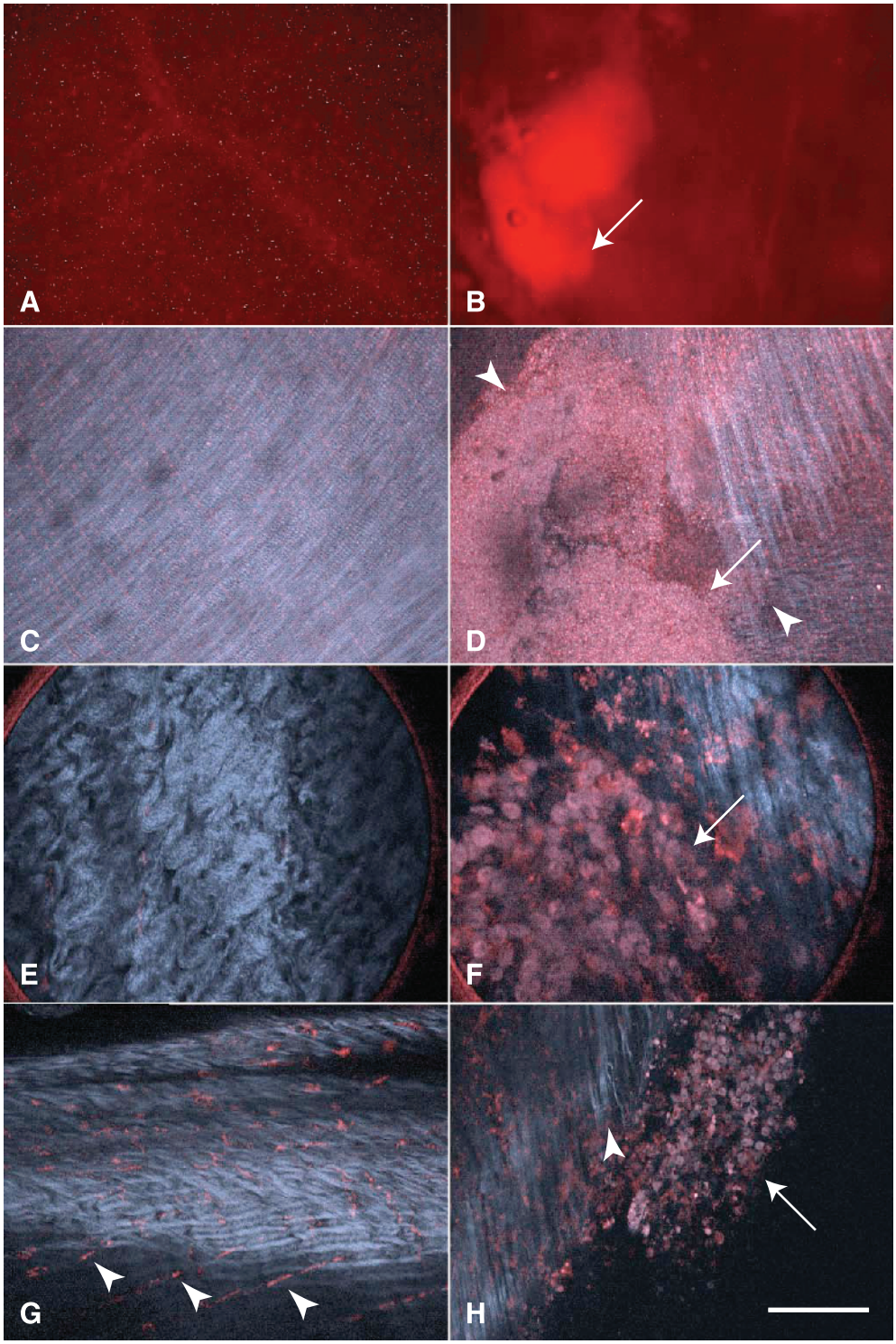

Figure 7. Imaging cathepsin activity using MPM/SHG. Images of the normal peritoneum (A, C, E, and G) and peritoneal tumors (B, D, F and H, arrows) from the disseminated peritoneal model after administration of ProSense 680 (red). Detection of neoplastic lesion using standard stereofluoroscopy (A and B) and subsequent mapping its tumor boundaries (D, arrowheads) in three dimensions with MPM/SHG. In this case, normal (C) and tumor (D) images were collected with a low-magnification objective (4×/0.28 NA) and displayed as projections, each from 100 images at 5-μm intervals. Discrimination between normal abdominal wall (E) and neoplasm (F) at cellular resolution with the stick objective. High-resolution MPM/SHG images demonstrate cathepsin activity in certain stromal cells (G, arrowheads) and neoplastic cells (H, arrow). In addition, they show alterations in the size and shape of neoplastic cells and tissue architecture as well as the orientation of collagen fibrils toward tumor boundary (H, arrowhead). Scale bars, 1000 μm (A, B), 500 μm (C, D), 80 μm (E, F), and 100 μm (G, H).

Secondly, MPM/SHG imaging allowed better estimation of location and characterization of collagenous stroma. Because metastatic progression of ovarian cancer is known to coincide with increased collagen synthesis and degradation [26,64], we analyzed images for an increase in segmental collagen associated with fibrillogenesis in the regions surrounding tumors but found comparable amounts. Instead, we observed a thickening of collagen at the basement membrane in early ovarian neoplasias and straighter, less uniform collagen fibrils around peritoneal neoplastic implants, consistent with previous reports that stromal matrix components become rearranged in tight, linearly aligned fibers in invasive ovarian carcinomas [65,66]. In addition, we demonstrated that most collagen fibers near the invasive edge are located perpendicular toward its surface. These results are consistent with previous reports from breast tumors [62], suggesting that fibrils oriented perpendicular to the tumor were correlated to tumor cell infiltration to the host stromal tissue.

Thirdly, MPM allows comprehensive evaluation of spectral changes in intrinsic fluorescence with cellular resolution. We determined that intensity and anisotropy analyses of tissues are unlikely to yield consistent results owing to their high sensitivity to tissue scattering. Similar to a previous report from human tissue [14], we detected a red shift in fluorescence of neoplastic cells in mice with advanced EOC. Kirkpatrick et al. [14] attributed this spectral shift to an increase in the overall FAD-to-NAD(P)H ratio. However, according to our observations, this alteration in intrinsic cellular fluorescence derives not from an average color change but from a specific population of redder-emitting cells within the tumor. These cells were determined to be alive by cellular NAD(P)H expression and calcein-AM staining and may represent porphyrin-containing cells [47,67,68].

Toward an In Vivo *Implementation of Intrinsic Tissue Fluorescence MPM/SHG*

Clearly, a standard multiphoton microscope cannot be used for microscopic imaging in humans. However, several new technologic advances have made an endoscopic version of MPM/SHG—a device for *in vivo* collection of histologic-like images—to be a realistically achievable goal. Several recently developed confocal endoscopes offer remarkable cellular-scale imaging *in vivo* and are undergoing clinical trials [69,70]. In these devices, motion artifacts are minimized with catheter tissue stabilization and use of suction ports. An endoscopic implementation of MPM may complement such efforts with the additional ability for imaging intrinsic tissue fluorescence and an expected several-fold increase in depth penetration [9]. The first challenge has been to engineer fibers through which sufficiently powerful femtosecond laser pulses can propagate with minimal temporal pulse broadening due to dispersion. An uncompensated 1-nJ, 100-fs pulse will lengthen to ~4000 fs after traveling through a meter of optical fiber (reducing the 2P excitation potential by a factor of 40). Pulse dispersion can be partially compensated at low powers. However, for higher power delivery, microstructured fibers are necessary. These are relatively large (keeping average intensities low) but only propagate a single mode because of the intricate boundary conditions [71,72]. Scanning is done either by wiggling the fiber [70,73–76] or through MEM devices [77] transferred to a gradient-index or microlens for focusing [78]. Several researchers have demonstrated collagen imaging through an MPM endoscope [77,79] but not yet *in vivo*. The real challenge has been to design an endoscope with the sensitivity for imaging intrinsic cellular fluorophores, which are typically 100-fold dimmer than standard fluorophores [12]. In the current study, we demonstrate cellular visualization *in vivo* using MPM/SHG of intrinsic emissions that can be used to identify neoplasias in several mouse models of ovarian cancer. In addition, we demonstrate the feasibility of an *in vivo* laparoscopic implementation of MPM/SHG by using a recently developed 3-mm-diameter stick objective that allows direct access to imaged tissues. In this case, a separate small tube served to stabilize and rinse the tissue, the latter capability being particularly relevant to tumors that present with internal bleeding.

Contrast Agents for Targeting MPM/SHG to Putative Neoplastic Lesions Regions

In addition to endogenous intrinsic fluorescence, it is likely that fluorescent contrast agents (e.g., ALA [80]) and/or smart indicators [42,81] will improve diagnostic information and signal once issues of toxicity and delivery are better understood. Others have demonstrated the utility of the cathepsin activity indicator ProSense 680 for ovarian cancer diagnostics [7]. We showed that this signal can be used to quickly identify lesions with standard fluoroscopy for subsequent cellular-resolved interrogation using MPM/SHG. ProSense 680 can be imaged simultaneously with intrinsic tissue emissions providing a contextual tissue background. Because it fluoresces in the NIR, ProSense 680 may also substantially improve the depth and accuracy to which lesions can be mapped with MPM/SHG in the difficult *in vivo* environment.

Taken together, our results demonstrate the feasibility of high-resolution imaging of epithelial ovarian cancer by laparoscopic nonlinear microscopy. They also demonstrate the value of MPM/SHG imaging for rapid initial assessment of ovarian cancer samples. Further advances in photonics and microfabrication should make it possible to produce an efficient fiber-coupled multiphoton endoscope with capabilities for a minimally invasive, all-optical biopsy for a cellularly resolved diagnostic assessment of ovarian cancer lesions as well as other malignancies.

Acknowledgments

The authors thank Jane An, Heather R. Martin, and Cynthia Kwong for excellent histotechnological and morphometric support and Dr Andrew Yen for providing a mouse c-Myc.

References

[1] Jemal A, Siegel R, Ward E, Hao Y, Xu J, and Thun MJ (2009). Cancer statistics, 2009. *CA Cancer J Clin* **59**, 225–249.
[2] Bast RC Jr, Hennessy B, and Mills GB (2009). The biology of ovarian cancer: new opportunities for translation. *Nat Rev Cancer* **9**, 415–428.
[3] Tingulstad S, Skjeldestad FE, Halvorsen TB, and Hagen B (2003). Survival and prognostic factors in patients with ovarian cancer. *Obstet Gynecol* **101**, 885–891.
[4] Olson SH, Mignone L, Nakraseive C, Caputo TA, Barakat RR, and Harlap S (2001). Symptoms of ovarian cancer. *Obstet Gynecol* **98**, 212–217.
[5] Zivanovic O, Aldini A, Carlson JW, and Chi DS (2009). Advanced cytoreductive surgery: American perspective. *Gynecol Oncol* **114**, S3–S9.
[6] Kosaka N, Ogawa M, Longmire MR, Choyke PL, and Kobayashi H (2009). Multi-targeted multi-color *in vivo* optical imaging in a model of disseminated peritoneal ovarian cancer. *J Biomed Opt* **14**, 014023.
[7] Sheth RA, Upadhyay R, Stangenberg L, Sheth R, Weissleder R, and Mahmood U (2009). Improved detection of ovarian cancer metastases by intraoperative quantitative fluorescence protease imaging in a pre-clinical model. *Gynecol Oncol* **112**, 616–622.
[8] Denk W, Strickler JH, and Webb WW (1990). Two-photon laser scanning fluorescence microscopy. *Science* **248**, 73–76.
[9] Zipfel WR, Williams RM, and Webb WW (2003). Nonlinear magic: multiphoton microscopy in the biosciences. *Nat Biotechnol* **21**, 1369–1377.

[10] Ramanujam N (2000). Fluorescence spectroscopy *in vivo*. In *Encyclopedia of Analytical Chemistry.* RA Meyer (Ed). John Wiley & Sons Ltd., Chihester, UK. pp. 20–56.

[11] Richards-Kortum R and Sevick-Muraca E (1996). Quantitative optical spectroscopy for tissue diagnosis. *Annu Rev Phys Chem* **47**, 555–606.

[12] Zipfel WR, Williams RM, Christie R, Nikitin AY, Hyman BT, and Webb WW (2003). Live tissue intrinsic emission microscopy using multiphoton-excited native fluorescence and second harmonic generation. *Proc Natl Acad Sci USA* **100**, 7075–7080.

[13] Helmchen F and Denk W (2005). Deep tissue two-photon microscopy. *Nat Methods* **2**, 932–940.

[14] Kirkpatrick ND, Brewer MA, and Utzinger U (2007). Endogenous optical biomarkers of ovarian cancer evaluated with multiphoton microscopy. *Cancer Epidemiol Biomarkers Prev* **16**, 2048–2057.

[15] Connolly DC, Bao R, Nikitin AY, Stephens KC, Poole TW, Hua X, Harris SS, Vanderhyden BC, and Hamilton TC (2003). Female mice chimeric for expression of the simian virus 40 TAg under control of the MISIIR promoter develop epithelial ovarian cancer. *Cancer Res* **63**, 1389–1397.

[16] Flesken-Nikitin A, Choi KC, Eng JP, Shmidt EN, and Nikitin AY (2003). Induction of carcinogenesis by concurrent inactivation of p53 and Rb1 in the mouse ovarian surface epithelium. *Cancer Res* **63**, 3459–3463.

[17] Corney DC, Flesken-Nikitin A, Godwin AK, Wang W, and Nikitin AY (2007). MicroRNA-34b and MicroRNA-34c are targets of p53 and cooperate in control of cell proliferation and adhesion-independent growth. *Cancer Res* **67**, 8433–8438.

[18] Flesken-Nikitin A, Toshkov I, Naskar J, Tyner KM, Williams RM, Zipfel WR, Giannelis EP, and Nikitin AY (2007). Toxicity and biomedical imaging of layered nanohybrids in the mouse. *Toxicol Pathol* **35**, 804–810.

[19] Kloppenburg P, Zipfel WR, Webb WW, and Harris-Warrick RM (2000). Highly localized Ca^{2+} accumulation revealed by multiphoton microscopy in an identified motoneuron and its modulation by dopamine. *J Neurosci* **20**, 2523–2533.

[20] Williams RM and Webb WW (2000). Single granule pH cycling in antigen-induced mast cell secretion. *J Cell Sci* **113** (Pt 21), 3839–3850.

[21] Flesken-Nikitin A, Williams RM, Zipfel WR, Webb WW, and Nikitin AY (2004). Use of multiphoton imaging for studying cell migration in the mouse. *Methods Mol Biol* **294**, 335–346.

[22] Davis B, Harleman JH, Heinrichs M, Maekawa A, McConnell RF, Reznik G, and Tucker M (2001). Female genital system. In *International Classification of Rodent Tumors. The Mouse.* U Mohr (Ed). Springer, Berlin Germany. pp. 211–268.

[23] Nikitin AY, Connolly DC, and Hamilton TC (2004). Pathology of ovarian neoplasms in genetically modified mice. *Comp Med* **54**, 26–28.

[24] Scully RE and Sobin LH (1999). *Histological Typing of Ovarian Tumours.* Berlin, Germany: Springer.

[25] Williams RM, Zipfel WR, and Webb WW (2005). Interpreting second-harmonic generation images of collagen I fibrils. *Biophys J* **88**, 1377–1386.

[26] Kenny HA and Lengyel E (2009). MMP-2 functions as an early response protein in ovarian cancer metastasis. *Cell Cycle* **8**, 683–688.

[27] Deligdisch L, Einstein AJ, Guera D, and Gil J (1995). Ovarian dysplasia in epithelial inclusion cysts. A morphometric approach using neural networks. *Cancer* **76**, 1027–1034.

[28] Deligdisch L and Gil J (1989). Characterization of ovarian dysplasia by interactive morphometry. *Cancer* **63**, 748–755.

[29] Deligdisch L, Gil J, Kerner H, Wu HS, Beck D, and Gershoni-Baruch R (1999). Ovarian dysplasia in prophylactic oophorectomy specimens: cytogenetic and morphometric correlations. *Cancer* **86**, 1544–1550.

[30] Deligdisch L, Miranda C, Barba J, and Gil J (1993). Ovarian dysplasia: nuclear texture analysis. *Cancer* **72**, 3253–3257.

[31] Gil J and Deligdisch L (1989). Interactive morphometric procedures and statistical analysis in the diagnosis of ovarian dysplasia and carcinoma. *Pathol Res Pract* **185**, 680–685.

[32] Yu Q and Heikal AA (2009). Two-photon autofluorescence dynamics imaging reveals sensitivity of intracellular NADH concentration and conformation to cell physiology at the single-cell level. *J Photochem Photobiol B* **95**, 46–57.

[33] Brown EB, Campbell RB, Tsuzuki Y, Xu L, Carmeliet P, Fukumura D, and Jain RK (2001). *In vivo* measurement of gene expression, angiogenesis and physiological function in tumors using multiphoton laser scanning microscopy. *Nat Med* **7**, 864–868.

[34] Condeelis J and Segall JE (2003). Intravital imaging of cell movement in tumours. *Nat Rev Cancer* **3**, 921–930.

[35] Rogart JN, Nagata J, Loeser CS, Roorda RD, Aslanian H, Robert ME, Zipfel WR, and Nathanson MH (2008). Multiphoton imaging can be used for microscopic examination of intact human gastrointestinal mucosa *ex vivo*. *Clin Gastroenterol Hepatol* **6**, 95–101.

[36] Gounaris E, Tung CH, Restaino C, Maehr R, Kohler R, Joyce JA, Ploegh HL, Barrett TA, Weissleder R, and Khazaie K (2008). Live imaging of cysteine-cathepsin activity reveals dynamics of focal inflammation, angiogenesis, and polyp growth. *PLoS One* **3**, e2916.

[37] Weissleder R and Ntziachristos V (2003). Shedding light onto live molecular targets. *Nat Med* **9**, 123–128.

[38] Weissleder R and Pittet MJ (2008). Imaging in the era of molecular oncology. *Nature* **452**, 580–589.

[39] Jonkers J and Berns A (2002). Conditional mouse models of sporadic cancer. *Nat Rev Cancer* **2**, 251–265.

[40] Van Dyke T and Jacks T (2002). Cancer modeling in the modern era: progress and challenges. *Cell* **108**, 135–144.

[41] Frese KK and Tuveson DA (2007). Maximizing mouse cancer models. *Nat Rev Cancer* **7**, 645–658.

[42] Pierce MC, Javier DJ, and Richards-Kortum R (2008). Optical contrast agents and imaging systems for detection and diagnosis of cancer. *Int J Cancer* **123**, 1979–1990.

[43] Avrillier S, Tinet E, Ettori D, and Anidjar M (1997). Laser-induced autofluorescence diagnosis of tumors. *Phys Scr* **T72**, 87–92.

[44] Brancaleon L, Durkin AJ, Tu JH, Menaker G, Fallon JD, and Kollias N (2001). *In vivo* fluorescence spectroscopy of nonmelanoma skin cancer. *Photochem Photobiol* **73**, 178–183.

[45] Coghlan L, Utzinger U, Richards-Kortum R, Brookner C, Zuluaga A, Gimenez-Conti I, and Follen M (2001). Fluorescence spectroscopy of epithelial tissue throughout the dysplasia-carcinoma sequence in an animal model: spectroscopic changes precede morphologic changes. *Lasers Surg Med* **29**, 1–10.

[46] Heintzelman DL, Utzinger U, Fuchs H, Zuluaga A, Gossage K, Gillenwater AM, Jacob R, Kemp B, and Richards-Kortum RR (2000). Optimal excitation wavelengths for *in vivo* detection of oral neoplasia using fluorescence spectroscopy. *Photochem Photobiol* **72**, 103–113.

[47] Li BH and Xie SS (2005). Autofluorescence excitation-emission matrices for diagnosis of colonic cancer. *World J Gastroenterol* **11**, 3931–3934.

[48] Majumder SK, Mohanty SK, Ghosh N, Gupta PK, Jain DK, and Khan F (2000). A pilot study on the use of autofluorescence spectroscopy for diagnosis of the cancer of human oral cavity. *Curr Sci* **79**, 1089–1094.

[49] Qu JNY, Chang HP, and Xiong SM (2002). Fluorescence spectral imaging for characterization of tissue based on multivariate statistical analysis. *J Opt Soc Am A Opt Image Sci Vis* **19**, 1823–1831.

[50] Qu JY, Wing P, Huang Z, Kwong D, Sham J, Lee SL, Ho WK, and Wei WI (2000). Preliminary study of *in vivo* autofluorescence of nasopharyngeal carcinoma and normal tissue. *Lasers Surg Med* **26**, 432–440.

[51] Ramanujam N, Mitchell MF, Mahadevan A, Warren S, Thomsen S, Silva E, and Richards-Kortum R (1994). *In vivo* diagnosis of cervical intraepithelial neoplasia using 337-nm-excited laser-induced fluorescence. *Proc Natl Acad Sci USA* **91**, 10193–10197.

[52] Wang TD, Crawford JM, Feld MS, Wang Y, Itzkan I, and Van Dam J (1999). *In vivo* identification of colonic dysplasia using fluorescence endoscopic imaging. *Gastrointest Endosc* **49**, 447–455.

[53] Zheng W, Lau W, Cheng C, Soo KC, and Olivo M (2003). Optimal excitation-emission wavelengths for autofluorescence diagnosis of bladder tumors. *Int J Cancer* **104**, 477–481.

[54] Georgakoudi I and Feld MS (2004). The combined use of fluorescence, reflectance, and light-scattering spectroscopy for evaluating dysplasia in Barrett's esophagus. *Gastrointest Endosc Clin N Am* **14**, 519–537, ix.

[55] Haringsma J, Tytgat GN, Yano H, Iishi H, Tatsuta M, Ogihara T, Watanabe H, Sato N, Marcon N, Wilson BC, et al. (2001). Autofluorescence endoscopy: feasibility of detection of GI neoplasms unapparent to white light endoscopy with an evolving technology. *Gastrointest Endosc* **53**(6), 642–650.

[56] Kobayashi M, Tajiri H, Seike E, Shitaya M, Tounou S, Mine M, and Oba K (2001). Detection of early gastric cancer by a real-time autofluorescence imaging system. *Cancer Lett* **165**, 155–159.

[57] Ikeda N, Hiyoshi T, Kakihana M, Honda H, Kato Y, Okunaka T, Furukawa K, Tsuchida T, Kato H, and Ebihara Y (2003). Histopathological evaluation of fluorescence bronchoscopy using resected lungs in cases of lung cancer. *Lung Cancer* **41**, 303–309.

[58] Cheong WF, Prahl SA, and Welch AJ (1990). A review of the optical-properties of biological tissues. *IEEE J Quantum Electron* **26**, 2166–2185 (with update at http://omlc.ogi.edu/pubs/pdf/cheong2190a.pdf).

[59] Chance B (2004). Mitochondrial NADH redox state, monitoring discovery and deployment in tissue. *Methods Enzymol* **385**, 361–370.
[60] Han X, Burke RM, Zettel ML, Tang P, and Brown EB (2008). Second harmonic properties of tumor collagen: determining the structural relationship between reactive stroma and healthy stroma. *Opt Express* **16**, 1846–1859.
[61] Mukherjee S, Wysock JS, Ng CK, Akhtar M, Perner S, Lee MM, Rubin MA, Maxfield FR, Webb WW, and Scherr DS (2009). Human bladder cancer diagnosis using multiphoton microscopy. *Proc Soc Photo Opt Instrum Eng* **7161**, 17–26.
[62] Provenzano PP, Inman DR, Eliceiri KW, Knittel JG, Yan L, Rueden CT, White JG, and Keely PJ (2008). Collagen density promotes mammary tumor initiation and progression. *BMC Med* **6**, 11.
[63] Skala MC, Squirrell JM, Vrotsos KM, Eickhoff JC, Gendron-Fitzpatrick A, Eliceiri KW, and Ramanujam N (2005). Multiphoton microscopy of endogenous fluorescence differentiates normal, precancerous, and cancerous squamous epithelial tissues. *Cancer Res* **65**, 1180–1186.
[64] Petri AL, Simonsen AH, Yip TT, Hogdall E, Fung ET, Lundvall L, and Hogdall C (2009). Three new potential ovarian cancer biomarkers detected in human urine with equalizer bead technology. *Acta Obstet Gynecol Scand* **88**, 18–26.
[65] Quiros RM, Valianou M, Kwon Y, Brown KM, Godwin AK, and Cukierman E (2008). Ovarian normal and tumor-associated fibroblasts retain *in vivo* stromal characteristics in a 3-D matrix-dependent manner. *Gynecol Oncol* **110**, 99–109.
[66] Yamada KM and Cukierman E (2007). Modeling tissue morphogenesis and cancer in 3D. *Cell* **130**, 601–610.
[67] Nilsson H, Johansson J, Svanberg K, Svanberg S, Jori G, Reddi E, Segalla A, Gust D, Moore AL, and Moore TA (1997). Laser-induced fluorescence studies of the biodistribution of carotenoporphyrins in mice. *Br J Cancer* **76**, 355–364.
[68] Onizawa K, Okamura N, Saginoya H, and Yoshida H (2003). Characterization of autofluorescence in oral squamous cell carcinoma. *Oral Oncol* **39**, 150–156.
[69] Lin KY, Maricevich M, Bardeesy N, Weissleder R, and Mahmood U (2008). *In vivo* quantitative microvasculature phenotype imaging of healthy and malignant tissues using a fiber-optic confocal laser microprobe. *Transl Oncol* **1**, 84–94.
[70] Smith LA, Tiffin N, Thomson M, Cross SS, and Hurlstone DP (2008). Chromoscopic endomicroscopy: *in vivo* cellular resolution imaging of the colorectum. *J Gastroenterol Hepatol* **23**, 1009–1023.
[71] Ouzounov D, Homoelle D, Zipfel W, Webb WW, Gaeta AL, West JA, Fajardo JC, and Koch KW (2002). Dispersion measurements of microstructured fibers using femtosecond laser pulses. *Optics Comm* **192**(3), 219–233.
[72] Ouzounov DG, Moll KD, Foster MA, Zipfel WR, Webb WW, and Gaeta AL (2002). Delivery of nanojoule femtosecond pulses through large-core microstructured fibers. *Opt Lett* **27**, 1513–1515.
[73] Bao H, Allen J, Pattie R, Vance R, and Gu M (2008). Fast handheld two-photon fluorescence microendoscope with a 475 microm × 475 microm field of view for *in vivo* imaging. *Opt Lett* **33**, 1333–1335.
[74] Delaney PM, King RG, Lambert JR, and Harris MR (1994). Fibre optic confocal imaging (FOCI) for subsurface microscopy of the colon *in vivo*. *J Anat* **184** (Pt 1), 157–160.
[75] Engelbrecht CJ, Johnston RS, Seibel EJ, and Helmchen F (2008). Ultra-compact fiber-optic two-photon microscope for functional fluorescence imaging *in vivo*. *Opt Express* **16**, 5556–5564.
[76] Myaing MT, MacDonald DJ, and Li X (2006). Fiber-optic scanning two-photon fluorescence endoscope. *Opt Lett* **31**, 1076–1078.
[77] Tang S, Jung W, McCormick D, Xie T, Su J, Ahn YC, Tromberg BJ, and Chen Z (2009). Design and implementation of fiber-based multiphoton endoscopy with microelectromechanical systems scanning. *J Biomed Opt* **14**, 034005.
[78] Barretto RP, Messerschmidt B, and Schnitzer MJ (2009). *In vivo* fluorescence imaging with high-resolution microlenses. *Nat Methods* **6**, 511–512.
[79] Fu L, Jain A, Xie H, Cranfield C, and Gu M (2006). Nonlinear optical endoscopy based on a double-clad photonic crystal fiber and a MEMS mirror. *Opt Express* **14**, 1027–1032.
[80] Loning MC, Diddens HC, Holl-Ulrich K, Loning U, Kupker W, Diedrich K, and Huttmann G (2006). Fluorescence staining of human ovarian cancer tissue following application of 5-aminolevulinic acid: fluorescence microscopy studies. *Lasers Surg Med* **38**, 549–554.
[81] Mahmood U and Weissleder R (2003). Near-infrared optical imaging of proteases in cancer. *Mol Cancer Ther* **2**, 489–496.